



THIS MANUSCRIPT HAS BEEN SUBMITTED TO THE JOURNAL OF GLACIOLOGY AND HAS NOT BEEN PEER-REVIEWED.

Mechanisms for upstream migration of firn aquifer drainage: preliminary observations of Helheim Glacier, Greenland

Journal:	<i>Journal of Glaciology</i>
Manuscript ID	JOG-2024-0076
Manuscript Type:	Article
Date Submitted by the Author:	01-Jul-2024
Complete List of Authors:	Mejia, Jessica; University at Buffalo, Geology Poinar, Kristin; University at Buffalo, Geology Meyer, Colin; Dartmouth College, Thayer School of Engineering Sommers, Aleah; Dartmouth College, Thayer School of Engineering Chu, Winnie; Georgia Institute of Technology
Keywords:	Crevasses, Polar firn, Wind-blown snow, Glacier modelling, Remote sensing
Abstract:	Surface meltwater can influence subglacial hydrology and ice dynamics if it reaches the ice sheet's base. Firn aquifers store meltwater and drain into wide crevasses marking the aquifer's downstream boundary, indicating water from firn aquifers drives hydrofracture to establish the upglacier-most surface-to-bed hydraulic connections. Yet, sparse observations limit our understanding of the physical processes controlling firn aquifer drainage. We assess the potential for future inland firn aquifer drainage migration with field observations and linear elastic fracture mechanics (LEFM) modeling to determine the conditions needed to initiate and sustain hydrofracture on Helheim Glacier, Greenland. We find that local stress conditions alone can drive crevasse tips into the firn aquifer, without meltwater, allowing hydrofracture initiation year-round. We infer inland expansion of crevasses over the firn aquifer from crevasse-nucleated whaleback dune formation and GNSS-station detected crevasse opening extending 14 km and 4 km, respectively, inland from

	<p>the current, farthest-upstream drainage point. Using our LEFM model, we identify three vulnerable regions with coincidence between dry crevasse depth and water table variability, indicating potential future inland firn aquifer drainage sites. These results suggest the downstream boundary of firn aquifers can migrate inland under future warming scenarios and may already be underway.</p>

SCHOLARONE™
Manuscripts

Mechanisms for upstream migration of firn aquifer drainage: preliminary observations of Helheim Glacier, Greenland

Jessica MEJIA,¹ Kristin POINAR,¹ Colin R. MEYER², Aleah SOMMERS², Winnie CHU³

¹*Department of Geology, University at Buffalo, Buffalo, NY, USA*

²*Thayer School of Engineering, Dartmouth College, Hanover, NH, USA*

³*School of Earth & Atmospheric Sciences, Georgia Institute of Technology, Atlanta, GA, USA*

ABSTRACT. Surface meltwater can influence subglacial hydrology and ice dynamics if it reaches the ice sheet's base. Firn aquifers store meltwater and drain into wide crevasses marking the aquifer's downstream boundary, indicating water from firn aquifers drives hydrofracture to establish the upglacier-most surface-to-bed hydraulic connections. Yet, sparse observations limit our understanding of the physical processes controlling firn aquifer drainage. We assess the potential for future inland firn aquifer drainage migration with field observations and linear elastic fracture mechanics (LEFM) modeling to determine the conditions needed to initiate and sustain hydrofracture on Helheim Glacier, Greenland. We find that local stress conditions alone can drive crevasse tips into the firn aquifer, without meltwater, allowing hydrofracture initiation year-round. We infer inland expansion of crevasses over the firn aquifer from crevasse-nucleated whaleback dune formation and GNSS-station detected crevasse opening extending 14 km and 4 km, respectively, inland from the current, farthest-upstream drainage point. Using our LEFM model, we identify three vulnerable regions with coincidence between dry crevasse depth and water table variability, indicating potential future inland firn aquifer drainage sites. These results suggest the downstream boundary of firn aquifers can migrate inland under future warming scenarios and may already be underway.

28 INTRODUCTION

29 Amplified Arctic warming has led to an increase in the the magnitude and inland extent of melting on
30 the Greenland Ice Sheet (van den Broeke and others, 2023). Meltwater contributes to ice sheet mass
31 loss directly, via runoff, and indirectly, via ice dynamic discharge, through modulating subglacial water
32 pressures and sliding once it reaches the ice sheet's base. Meltwater can be transferred from the ice sheet
33 surface to bed through the hydraulic fracture of crevasses to the bed. With a sufficient meltwater supply,
34 full-thickness crevasses can transport large volumes of water to the most hydraulically efficient parts of
35 the subglacial drainage system (Gulley and others, 2012). These surface-to-bed hydraulic connections are
36 more prevalent at low elevations, and decline with distance inland on the ice sheet (Phillips and others,
37 2011; Yang and Smith, 2016). Far inland, these connections are located in the accumulation area where
38 high-elevation melting in snow-covered areas can also form full-thickness crevasses (Poinar and others,
39 2015).

40 High on the ice sheet above the ELA, snow-cover persists for all or much of the year. Meltwater
41 percolates down through the snowpack, and in areas with high winter accumulation rates the thick annual
42 snow layer protects liquid water from refreezing and allows the formation of firn aquifers that perennially
43 store liquid water beneath the snow surface (Forster and others, 2014). Firn aquifers are thermally bounded
44 at their base and are resupplied with surface meltwater that percolates down through the snow and firn
45 to recharge the aquifer before laterally flowing downslope through the firn pore space (Meyer and Hewitt,
46 2017). If a crevasse intersects a firn aquifer, water discharge from the firn aquifer into the crevasse can drive
47 full-thickness hydrofracture (Poinar and others, 2017), bringing water directly to the subglacial drainage
48 system and establishing the upglacier-most surface-to-bed hydraulic connections along a given flow line
49 (Cicero and others, 2023).

50 Climatic warming has caused the GrIS to experience melt at higher elevations, resulting in the seasonal
51 snowline retreating to higher elevations (Steger and others, 2017b). This high elevation melting has similarly
52 caused the upstream boundary of Greenland firn aquifers to migrate inland (Horlings and others, 2022;
53 Miège and others, 2016; Miller and others, 2020). We investigate the hypothesis that the downstream
54 boundary of the firn aquifer is also changing. The location where firn aquifers drain is important because
55 firn-aquifer water within the subglacial drainage system elevates water pressures over large areas (>10 km)
56 and can influence ice velocity and the seasonal evolution of and water residence times within the downstream

57 drainage system (Poinar and others, 2019). Ultimately, firn aquifer drainage at higher-elevations would
58 supply aquifer-sourced water to new regions of the bed which has the potential to influence subglacial
59 water pressures, ice velocity, and downstream drainage system evolution with potentially widespread and
60 significant ramifications for ice dynamics and ultimately mass loss (Bartholomew and others, 2011; Doyle
61 and others, 2014; Mejia and others, 2022; Poinar and others, 2015; Sommers and others, 2024).

62 To test our hypothesis that the drainage region of firn aquifers can move inland, an understanding of the
63 physical processes controlling the formation of firn-aquifer draining crevasses is required. While initial work
64 found that firn aquifers have the ability to drive full-thickness hydrofracture (Poinar and others, 2017),
65 the initiation of hydrofracture is poorly constrained due to the difficulty of collecting direct observations.
66 To address this gap, we investigate the requirements for firn aquifer fed hydrofracture initiation using
67 linear elastic fracture mechanics (LEFM), complemented with in situ and satellite-derived observations, to
68 calculate dry crevasse depths for a region on Helheim Glacier to determine if crevasses can penetrate the
69 firn aquifer upon formation. We interpret our results to evaluate the potential for the inland migration of
70 the region draining the firn aquifer under future climatic warming.

71 METHODS

72 Field site

73 Helheim Glacier is a fast-flowing outlet glacier in southeast Greenland with an extensive firn aquifer located
74 in the accumulation area spanning elevations of 1,400 to 1,800 m a.s.l. (Fig. 1a). Here, we focus on a 23 km
75 segment along an approximate flow line on the southern branch of Helheim Glacier (Fig. 1). This specific
76 region was chosen to align with repeat firn aquifer locations detected by NASA's Operation IceBridge (OIB)
77 between 2010–17 (Miège and others, 2016) and existing data from geophysical field campaigns undertaken
78 during 2015 and 2016 (Miller and others, 2017, 2018; Montgomery and others, 2017). In June 2023 we
79 established a camp (66.3538°N, -39.1560°E) located 4 km upglacier from the crevasse field bounding the
80 firn aquifer (Fig. 1). We installed eight Global Navigation Satellite System Stations (GNSS) in a strain
81 diamond configuration that extended from our base camp to the crevasse field in June and July 2023 (Fig.
82 1a). We now briefly describe our remote sensing analysis and field measurements. A description of our
83 linear elastic fracture mechanics (LEFM) model in Appendix B.

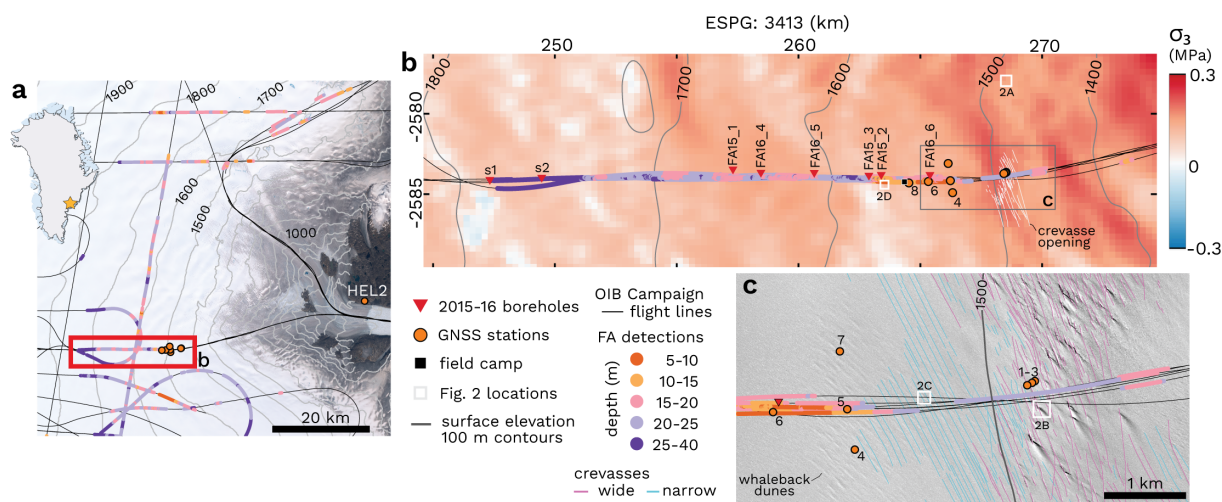


Fig. 1. (a) Study area location (red box) on Helheim Glacier's southern branch with OIB firn aquifer locations (dots colored as depth) along flight lines (narrow black lines). Ice surface elevation contours in m.a.s.l. accessed through BedMachine v3 based on Greenland Ice Mapping Project DEMs (Howat and others, 2014; Morlighem and others, 2017). Inset shows location in southeast Greenland. (b) Firn aquifer profile with principal strain rates (σ_3) in MPa. On-ice GNSS stations (orange circles) and historic firn aquifer sampling sites (red triangles) are marked along profile, surface elevation contours in m above WGS84 ellipsoid (Porter and others, 2023). (c) Detail (5 km x 3 km) of narrow (blue) and wide (pink) crevasses delineated on 28 March 2024 WorldView-2 imagery.

84 Firn aquifer detection

85 We use firn aquifer locations detected by NASA Operation IceBridge (OIB) accumulation radar (AR) data
 86 over the years 2010–17 (Miège and others, 2016; Miège, 2018), which locate the depth of the firn aquifer
 87 water table—the upper surface of saturated firn layer—beneath the snow surface (Fig 1a). Specifically, we
 88 use a subset of data from Miège and others (2016), the surface elevation and firn aquifer depth observed at
 89 repeat flight lines covering the 23 km segment of the firn aquifer intersecting our field site (Fig. 1b). OIB
 90 flight lines maintained spatial consistency between years with a maximum offset of 250 m in the north-south
 91 (across-flow) direction. Small deviations in campaign flight track, winter snow accumulation, and survey
 92 date introduced variability in surface elevation measurements between years (standard deviation, $\text{std}=3.4$
 93 m). Notably, ice sheet surface elevations observed in 2010 and 2011 were consistently higher than all other
 94 years. To reduce variability in surface elevation between years we apply a correction of -4.0 m for 2010,
 95 and -3.0 m for 2011 data, amounting to the average surface elevation offset from 2016. This correction
 96 is imperative because the ice sheet surface elevation acts as a datum when converting the aquifer water
 97 table depth to water table elevation and we use 2016 surface elevations as our reference for calculated dry

98 crevasse depth. Failure to adjust for 2010–11 offsets could erroneously imply a reduced water table depth
99 when comparing 2010–11 water table elevations to the 2016 ice sheet surface. Water table depth is reported
100 in meters below the ice sheet surface and has an associated measurement uncertainty of ± 72 cm (Miège
101 and others, 2016). Aquifer thickness and bottom elevation are extrapolated from 2016 surface elevations
102 and point observations of aquifer water table and bottom depths measured in 2015 and 2016 (Fig. 1b;
103 Montgomery and others, 2017).

104 **Stress regime and crevasse detection**

105 We use kinematic site positions for our three on-ice GNSS stations to calculate strain rates between station
106 pairs. We supplement these point-measurements with calculated primary principal strain rates using NASA
107 MEaSUREs program Multi-year Greenland Ice Sheet Velocity Mosaic (Joughin and others, 2016) velocities.
108 This velocity product comprises a year-round velocity average that is selected to be representative of the
109 1995–2015 period and has a pixel size of 250 m by 250 m. Our GNSS station deployment, data analysis,
110 and primary principal strain rate calculations are described fully in Appendix A.

We smooth station positions using a three-hour centered rolling average. We then calculate strain rates
between station pairs HLM8-HLM6 and HLM6-HLM5 from 15-minute downsampled station positions.
Specifically, we calculate daily logarithmic strain rate, $\dot{\epsilon}$, for a rolling window applied to the 15-minute
station positions.

$$\dot{\epsilon} = \frac{1}{\Delta t} \ln \frac{\ell_1}{\ell_0} \quad (1)$$

111 where Δt is 24 hours, ℓ_0 and ℓ_1 are station separation in meters at the beginning and end of the 24 hour time
112 span, respectively. This technique produces strain rates between station pairs at a 15-minute frequency at
113 times when 24-hour separated data are available for each station.

114 *Crevasse identification from satellite imagery*

115 We manually located crevasses across our study area using WorldView imagery acquired between 2015
116 and 2023. We use 13 WorldView-1 panchromatic scenes with a ~ 0.5 m resolution, and two WorldView-2
117 multi-spectral scenes with a ~ 2 m resolution. Satellite geolocation accuracy is reported at ~ 5.0 m CE90
118 without ground control (Maxar, 2021), however, through comparison between features in WorldView and
119 Landsat images we estimate a geodetic location accuracy of 80 m, a similar finding as Poinar and Andrews
120 (2021). Crevasses were user-identified in QGIS for one acquisition date at a time and a digitizing radius

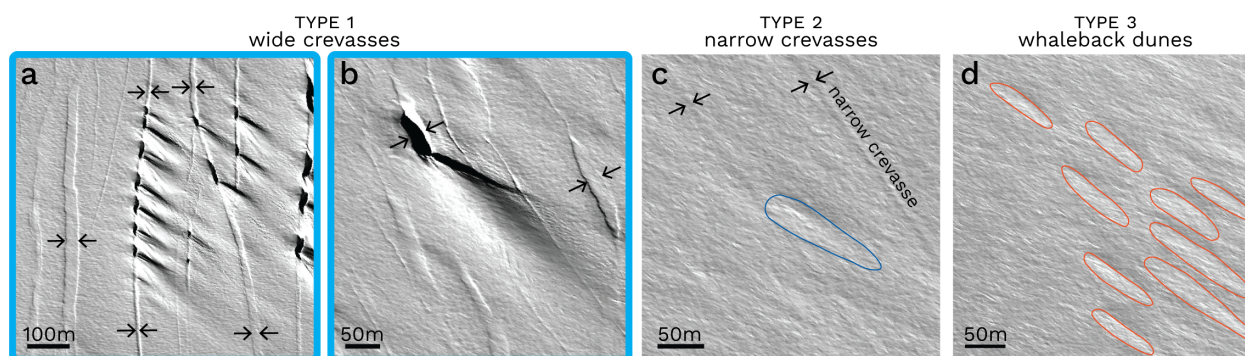


Fig. 2. Accumulation area crevasses with whaleback dunes. Wide crevasses ($>5\text{m}$) with multiple (a) and a single (b) dune. Arrows point to crevasses and blue boxes denote wide hydrofractured crevasses. Type 2 (c) narrow crevasses with a single dune (blue), and Type 3 (d) dunes (orange) without a visible nucleating crevasse. Imagery locations are marked in white with corresponding labels in Fig. 1b-c.

121 of greater than two meters. We searched for crevasses using a screen scale of 1:10,000 within the region
 122 coinciding with the firn aquifer extent determined by Miège and others (2016). We divide accumulation
 123 area crevasses into three categories: (1) groups of crevasses with widths greater than five meters (Fig.
 124 2c–d), (2) narrow crevasses that appear as linear features and have widths on the order of one to two
 125 meters (Fig. 2b), and (3) crevasse-related longitudinal whaleback dunes where the nucleating crevasse is
 126 not visible in satellite imagery (Fig. 2a). We explain our reasoning for class 3 below.

127 Whaleback dunes are depositional snow bedforms created in regions with strong winds above $\sim 15\text{ m s}^{-1}$
 128 and elongated parallel to the wind direction (Kobayashi, 1980). We can envision two potential scenarios
 129 for the formation of whaleback dunes in Helheim Glacier's accumulation area. In the first scenario, dunes
 130 form on flat terrain whereby layers of wind-packed snow build up and erode throughout the winter, forming
 131 sastrugi. In this case, dunes and sastrugi have similar dimensions (lengths $\sim 10\text{ m}$), with whaleback dunes
 132 forming when a dune becomes polished and rounded on top, and can achieve lengths of up to 20 m (Li and
 133 Sturm, 2002). In the second scenario, whaleback dunes form when snow is transported under high wind
 134 speeds until it is deposited on the lee side of a sharp break on the snow surface. Dunes formed under this
 135 process are large, having widths over 10 m and lengths over 100 m (Filhol and Sturm, 2015), and persistent
 136 because erosion will rarely remove the feature after deposition (Li and Sturm, 2002). We observe both
 137 types of whaleback dunes on Helheim Glacier. The first type is small ($<20\text{ m}$) and ubiquitous, the second
 138 type is large ($>100\text{ m}$) and forms when wind-deposited snow accumulates on a crevasse wall from the
 139 created discontinuity in the snow surface of any size, even less than two meters (Fig. 2). We therefore use

140 the presence of large (lengths >100 m) whaleback dunes as a proxy for the existence of the small crevasses
141 that are undetectable in WorldView imagery.

142 **LEFM model for dry crevasse depth**

143 We calculate dry crevasse depth along OIB flight lines where a firn aquifer was detected by Miège and
144 others (2016) (Fig. 1a). The LEFM model used to determine dry crevasse depth is informed by primary
145 principal stress (Fig. 3a,b) at points along OIB flight lines. We use the field-calibrated model parameters
146 for the low-density firn layer surface density of $\rho_s = 400 \text{ kg m}^{-3}$ (A4) and a 50 m average crevasse spacing
147 identified from satellite imagery ($2W = 50 \text{ m}$). We compare initial dry crevasse depth to 2010–17 firn
148 aquifer water table elevations to determine inland areas potentially vulnerable to future hydrofracture,
149 using observations of crevasse opening and distribution changes to show that the stress conditions required
150 for crevasse formation are already being met over the firn aquifer.

151 **RESULTS**

152 **Dry crevasse depth**

153 We calculate dry crevasse depth from the primary principal stress at locations where a firn aquifer was
154 identified along OIB flight lines (Figs. 1a, 3a–b; Miège and others, 2016). Figure 3c–d shows OIB surface
155 elevation, 2010–17 firn aquifer surface elevation (Miège and others, 2016), approximated firn aquifer depth
156 extrapolated from 2015–16 in situ observations (Montgomery and others, 2017), and LEFM calculated dry
157 crevasse depth. In the one-kilometer wide main crevasse field, dry crevasses will penetrate $27.3 \pm 0.9 \text{ m}$,
158 which is deep enough to intersect the aquifer water table $22.7 \pm 0.6 \text{ m}$ below the snow surface in 2016 (Fig.
159 3c–d). Peak surface stress occurs along a 250 m wide area along our profile and produces the deepest
160 crevasses which penetrate 28.3 m in this area (Fig. 3b). The location of these peak stresses and deepest
161 crevasses immediately precedes the onset of active crevasse widening identified from WorldView image-
162 pairs over 2015–23 (white lines in Fig. 3a). On the longitudinal boundaries of the main crevasse field, dry
163 crevasse depth decreases until becoming equivalent to the water table depth (left of blue shaded area in
164 Fig. 3).

165 Dry crevasse penetration depth decreases with distance upglacier from the main crevasse field, following
166 the surface stress distribution (Figs. 3d). The upglacier edge of the main crevasse field marks a 1.5 km
167 region of narrow crevasses that extends to GNSS station HLM5 (Figs. 1c, 3a). At this intersection,

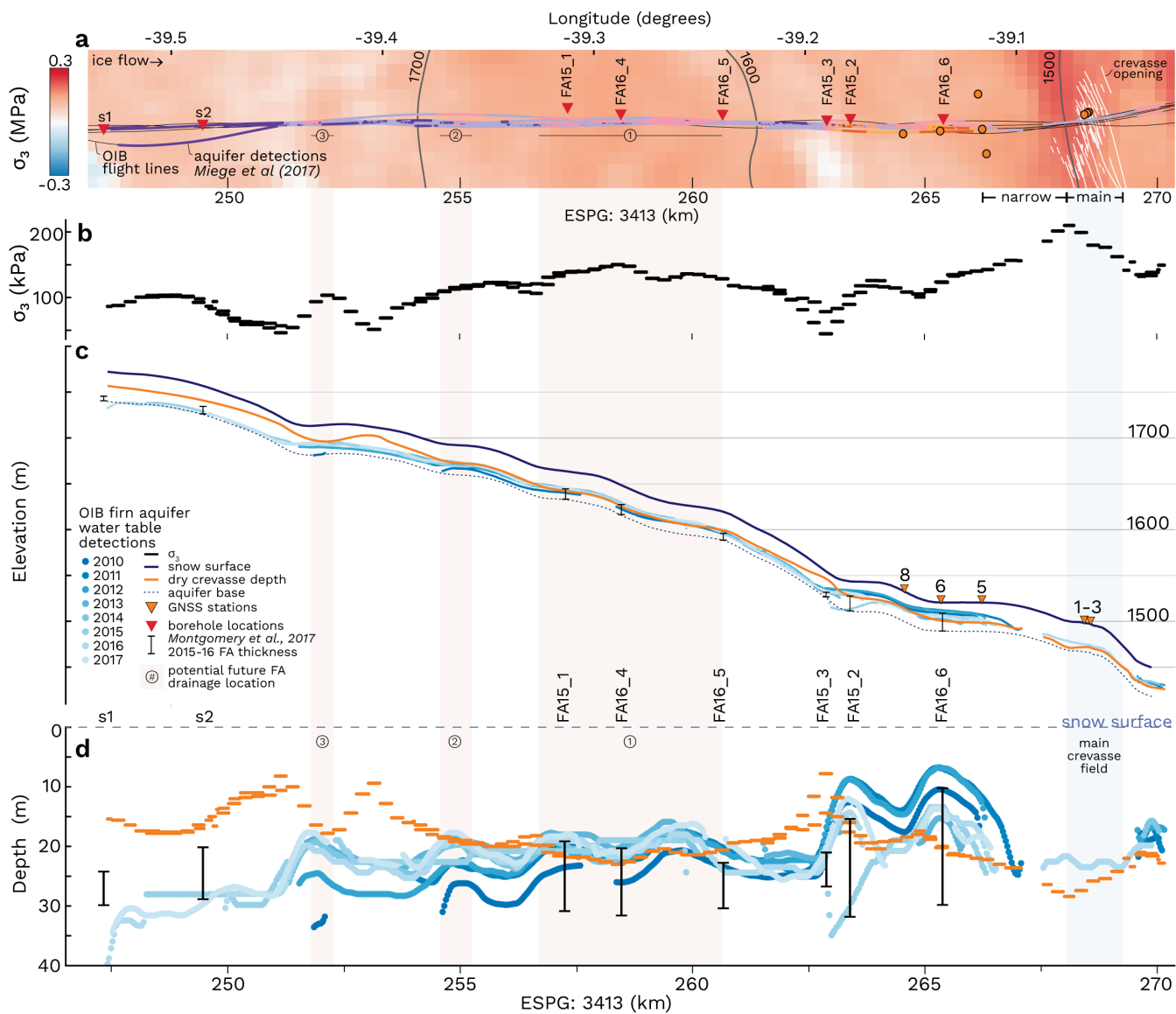


Fig. 3. (a) Plan-view of OIB flight lines and firn aquifer locations with background stress field, colors and symbology as in Fig. 1. (b) Primary principal stress along OIB flight lines in MPa. (c) LEFM dry crevasse depth calculations plotted in meters above WGS84 ellipsoid showing 2016 snow surface (black) and dry crevasse penetration depth (orange). OIB water table locations, 2015–16 aquifer measurements (Montgomery and others, 2017), and extrapolated aquifer bottom. (d) Same as (c) with data plotted as depth below snow surface in meters.

168 crevasse depth reaches the water table depth of 23.2 m and decreases over 1.5 km, reaching 21.0 m.
169 The firn aquifer's water level in this area are sparse and variable. Inspection of Accumulation Radar and
170 Multichannel Coherent Radar Depth Sounder radiograms confirm this gap in aquifer locations, likely caused
171 by a combination of the heavily crevassed area and a thin aquifer potentially caused by drawdown from
172 the nearby crevasses draining the firn aquifer, both of which would obscure the water table in radiograms.
173 Importantly, the lack of a detectable water table in this area does not mean that the aquifer is nonexistent;
174 instead, it means AR does not see the water table in these areas due to the aforementioned limitations of
175 the instrument itself. The firn aquifer's surface elevation falls below calculated crevasse depths 0.53 km,
176 1.09 km, or 1.29 km from the upglacier end of the main crevasse field corresponding to 2011, 2016, and 2015
177 OIB observations, respectively. The region 3.2 km upglacier from this point the water table reaches its
178 shallowest depths with a minimum depth of 6.7 m below the snow surface in 2011 and 2012. Due to these
179 shallow aquifer depths (>20 m), dry crevasses with depths of 11.8–22.0 m could penetrate the water table
180 in this area. The shallowest water table was located near GNSS station HLM6 and the aquifer sampling
181 site FA16_6 where Montgomery and others (2017) recorded a firn aquifer depth of 10 m below the snow
182 surface with a thickness of 20 m (Fig 3d).

183 In the upper 15.5 km upglacier-most region of our profile (west of FA15_3 at elevations above 1550
184 m) dry crevasse depth is predominately above the aquifer water table except for three areas where dry
185 crevasse depth falls within or comes close to the range of water table variability of 2010–17. The first
186 region spans 4 km between FA16_5 and FA15_1 where dry crevasse depth is deeper than the aquifer water
187 table in 2011–17 and is located 7.8 km from the main crevasse field (Fig. 3a,d). The second region spans
188 170 m where the water table reaches a local minima of 17.7–26.9 m and is located 12.7 km from the main
189 crevasse field at an elevation of 1,692 m. In 2017 and 2013 the water table height of 17.7 m and 18.0 m,
190 respectively, is within a meter of the dry crevasse depth of 17–17.4 m. The third region spans 370 m and
191 is located 15.7 km upglacier from the main crevasse field at an elevation of 1,714 m (Fig. 3b–d). The
192 minimum water table depth ranges from 18.7 m to 33.6 m which is within 1.0 m of dry crevasses with a
193 maximum depth of 17.7 m. This region corresponds with the upglacier firn aquifer extent in 2010, and
194 2012–13. In 2015–17 the firn aquifer extended 4.3 km further inland, reaching an elevation of 1,770 m, the
195 final 2.8 km is located in an extensional stress regime with dry crevasse depths ranging from 14–17 m. The
196 water table in this area was consistently below dry crevasse depths with OIB reported depths of 26.8–39.7
197 m and field measurements of 24 m at s1 and 20 m at s2 (Fig. 3c–d).

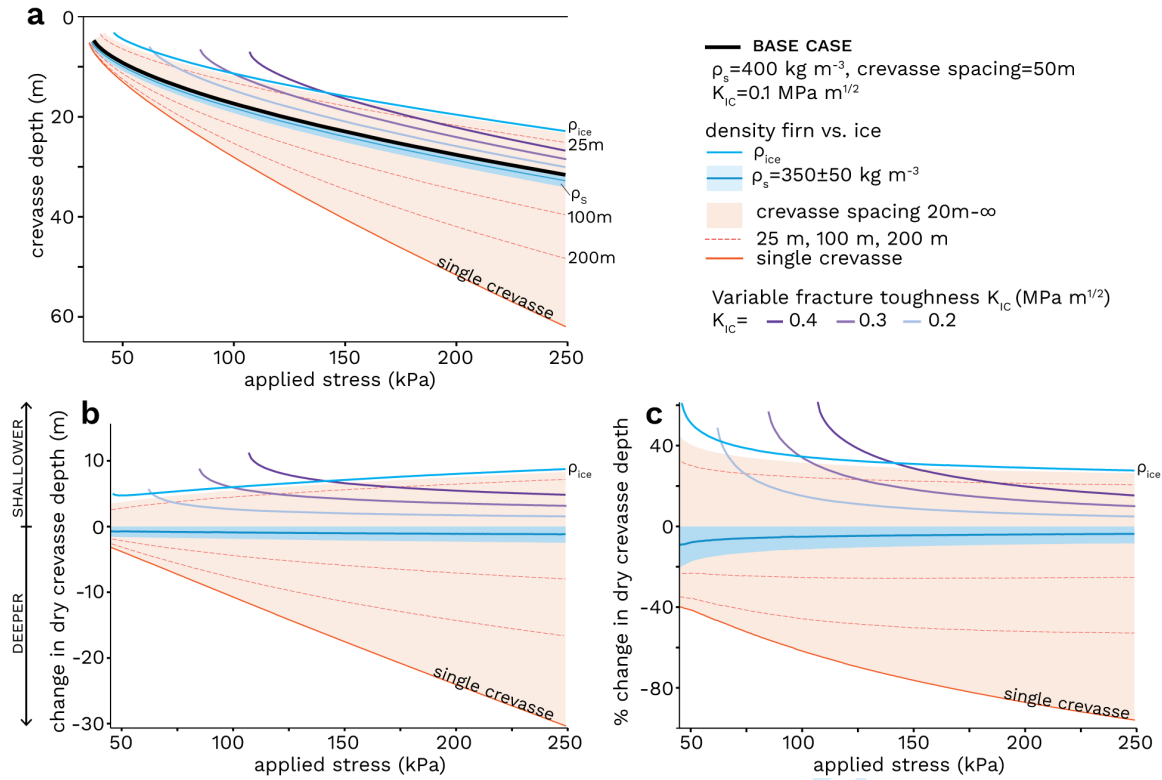


Fig. 4. (a) Dry crevasse depth for model parameters (see legend) for applied stress. (b) Change in dry crevasse depth from base case in meters and (c) as a percent difference from base case. Parameters explored are firn density (blue shading), ice density (blue line), crevasse spacing (orange shading and lines), and increasing K_{IC} (purple).

198 *Sensitivity to parameter values*

199 Here we report the range of dry crevasse depths that would be obtained with other plausible parameter
200 values different than our base case. A low-density firn layer reduces the lithostatic compressive stress
201 acting to close the crevasse, and produces deeper crevasses than for a constant ice density. We used a
202 depth varying density profile with a surface density of 400 kg m^{-3} , a crevasse spacing of 50 m, and fracture
203 toughness $K_{IC} = 0.1 \text{ MPa m}^{1/2}$ to obtain the results presented in the previous section (black line in Fig.
204 4a). If we instead used a constant ice density of 917 kg m^{-3} , under an applied stress $R_{xx}=45\text{--}250 \text{ kPa}$,
205 dry crevasses would be 4.7–8.8 m (61–27%) too shallow. Alternatively, a lower surface density of 300 kg
206 m^{-3} would produce dry crevasses 1.6–2.5 m (20–8%) deeper than our base case (Fig. 4).

207 The influence of multiple closely spaced crevasses, however, shields each crevasse from the far-field
208 resistive stress acting to open the crevasse, and produces shallower crevasses than for a single crevasse.
209 In our study area, crevasses readily identifiable from satellite imagery (i.e., type 1 and 2 crevasses) are
210 located in distinct crevasse fields with closely spaced crevasses, separated by 20–200 m with an average
211 spacing of 50 m along our profile. Crevasses become shallower as they are spaced closer together. For
212 example, a single, isolated crevasse formed under an applied stress of 45–250 kPa would be 2.3–30.3 m
213 (40–96%) deeper than our base case with a crevasse spacing of 50 m. Crevasses 100 m apart would be
214 23–25% or 1.5–8.0 m deeper than our base case, whereas crevasses 20 m apart would be 45–26% or 3.7–8.3
215 m more shallow (Fig. 4). Finally, larger values of K_{IC} would produce more shallow crevasses, such that
216 for $K_{IC}=0.4 \text{ MPa m}^{1/2}$ dry crevasses would be 62–15% or 11–4.8 m more shallow than our base case. The
217 minimum applied stress required for a crevasse to exist increases from 37 kPa to 107 kPa for $K_{IC}=0.1$ and
218 $0.4 \text{ MPa m}^{1/2}$, respectively (Fig. 4). Overall, we find that plausible parameter values are likely to change
219 our resulting dry crevasse depth by up to 20 m (Fig. 4). This uncertainty increases with background stress
220 and, at higher stresses, is asymmetric in depth: crevasses may be up to 20 m deeper than our base case,
221 but no more than 10 m shallower.

222 **Crevasse opening and distribution**

223 *GNSS station observations*

224 We report on data from the three upglacier-most center-line stations from our strain-diamond deployment.
225 The two upglacier-most GNSS stations, HLM8 and HLM6, captured crevasse opening on 25 June 2023,

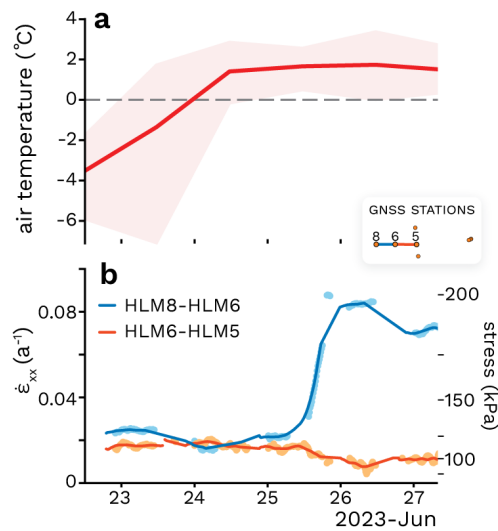


Fig. 5. Crevasse opening during 2023 melt onset (a) MERRA-2 derived mean air temperature for our field site with daily minimum and maximum values shaded. Grey dashed line marks 0°C. (b) GNSS measured strain rate between station pairs HEL8 to HLM6 (blue) and HLM6 to HLM5 (orange) with 15-minute observations (points) and smoothed (lines) data. Right axis shows strain rates converted to stress in kPa. Legend shows GNSS station configuration. Times are reported in local time.

226 within three days of the onset of melting at our field site (Fig. 5). MERRA-2 air temperatures for our study
 227 area remained above 1°C from 24–28 June 2023, marking the first multi-day period with above-freezing
 228 air temperatures for the 2023 melt season (Fig. 5a; additional details in Appendix A). This warm period
 229 coincided with an abrupt increase in the strain rate between the station pair HLM8–HLM6, whereby the
 230 strain rate increased from 0.057 a^{-1} to 0.877 a^{-1} between 13:30 and 19:30 local time (UTC-02:00) on 25
 231 June 2023. This strain corresponds to a lengthening of 3.4 ± 2.0 cm over the 790.3 m length span between
 232 stations. The abruptness of the lengthening makes it unlikely to be caused by viscous stretching of the
 233 ice. We consider the alternative interpretation, that this signal resulted from fracture, the opening of a
 234 3.4 ± 2.0 cm wide crevasse located at some position between stations HLM8 and HLM6. This fracture would
 235 have formed upon shear stress of 125–141 kPa (Fig. 5b), calculated with A for ice of -10°C in Eq. A1.
 236 From visual inspection of the raw data, we were not able to resolve multiple distinct opening events as
 237 could be produced by several crevasses opening in quick succession, but we cannot completely rule out this
 238 possibility.

239 The jump in the strain rate detected by HLM8–HLM6 was not reflected in the measurements by the
 240 downglacier station pair HLM6–HLM5. Over this same time period, strain rates between HLM6–HLM5

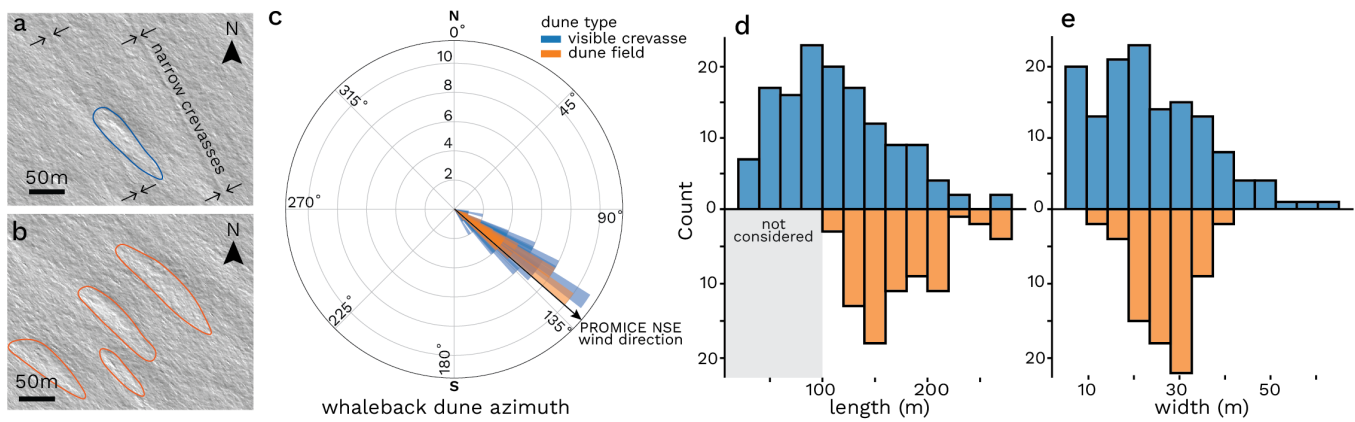


Fig. 6. Whaleback Dune Geometry. Whaleback dune examples (a) with and (b) without a visible crevasse in WorldView Imagery acquired 28 March 2023. Annotations as in Fig 2. Dune geometry comparison for dunes with (blue) and without (orange) visible crevasses. The black arrow marks wind direction during high wind events at the PROMICE weather station NSE. (c) Dune orientation histogram as azimuth angle in degrees from North (0°). Histograms for whaleback dune (d) length and (e) width in meters.

241 slightly decreased from 0.0157 a^{-1} to 0.0093 a^{-1} . We did not observe any significant net lengthening
 242 between stations HLM6–HLM5 accompanying the change in strain rates during the crevasse opening event
 243 which amounted to 0.5 mm over the 896.2 m length span between stations, which is below our measurement
 244 confidence. Therefore, we interpret strain rates between HLM6–HLM5 during this period as representative
 245 of typical slow viscous deformation.

246 *Crevasse distribution*

247 Crevasses with whaleback dunes (Fig. 2) are abundant in our study area of Helheim Glacier. Large
 248 whaleback dunes form on the downwind side of crevasses, where wind-blown snow is deposited on the
 249 discontinuity produced by the crevasse, to create dunes that then sinter in place and can achieve lengths
 250 exceeding 100 m. These whaleback dunes have been identified in OIB Digital Mapping System imagery
 251 by Poinar and others (2017), we therefore have some confidence in extrapolating them to smaller, sub-
 252 WorldView-pixel-scale crevasses. Because crevasses are required for the formation of whaleback dunes on
 253 Helheim Glacier (henceforth referred to as simply dunes), the presence of a dune without an observable
 254 crevasse suggests that either the crevasse is less than 0.4 m wide and is therefore undetectable on satellite
 255 imagery or the crevasse had formed then subsequently closed between the time of formation and image
 256 acquisition. Dunes with and without visible crevasses have similar orientations and geometries to each

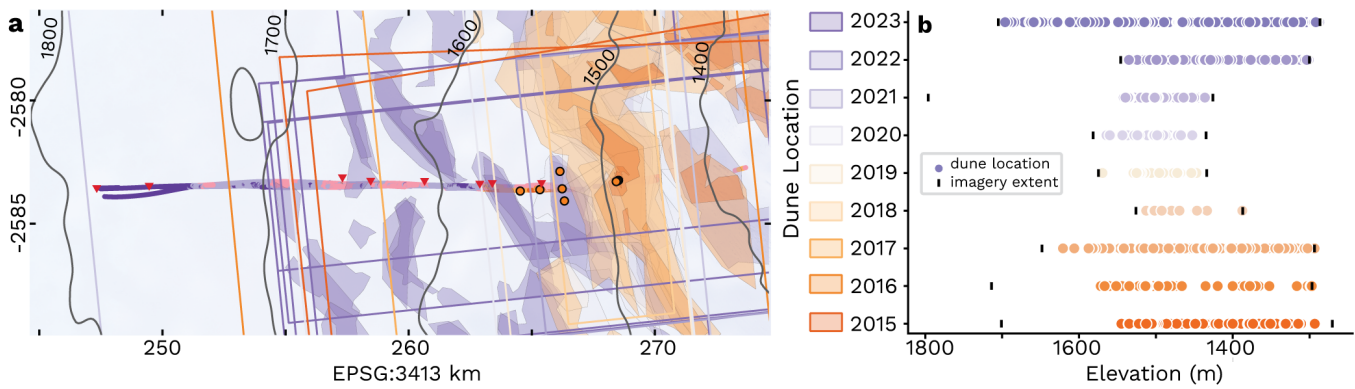


Fig. 7. Dune and crevasse locations 2015–24. (a) Map view of dune and crevasse locations with imagery extent delineated by solid lines. (b) Dune and crevasse elevations in meters above the WGS84 ellipsoid. Satellite imagery extent is marked by back bars.

257 other (Figure 6c) and with the median wind direction during high wind speed events ($>15 \text{ m s}^{-1}$) recorded
 258 by the PROMICE weather station NSE (Appendix A). The shorter lengths of dunes with visible crevasses
 259 can be attributed to our conservative approach in delineating dunes without visible crevasses producing
 260 calculated geometries for the larger dunes in dune fields (Fig. 6b). The close spacing of large crevasses on
 261 Helheim glacier contributes to the shorter dune lengths because neighboring crevasses frequently truncate
 262 dunes created by crevasses upwind. We therefore use the criteria of dunes with lengths greater than 100
 263 m to distinguish dunes without visible nucleating crevasses.

264 We observed dunes up to 13 km inland from our main crevasse in 2023 WorldView imagery, at elevations
 265 up to 1,696 m (Fig. 7). The dunes were present in four WorldView imagery scenes acquired from 21 March
 266 through 08 September 2023; they were not present in the preceding scene captured 12 April 2022, indicating
 267 dune field formation occurrence over the 344 days separating observations. Dunes maintained the same
 268 relative sizes and ~ 55 m spacing, and occupied the same areas in WorldView imagery acquired through
 269 08 September 2023. Because the 2023 inland extent of dunes was limited by WorldView imagery bounds
 270 (Fig. 6), dunes were likely present further inland and at higher-elevations than the 1,696 m reported here
 271 during 2023.

272 DISCUSSION

273 Our application of LEFM modeling to the crevasses in our study area showed that dry crevasses in suffi-
 274 ciently extensional stress settings can reach the depth of the firn aquifer water table, without the need for

275 surface melt. When these crack tips reach the water table, the inflow of firn aquifer water is likely sufficient
276 to hydrofracture to the bed (Poinar and others, 2017). Thus, we find that water table height and stress
277 state determine whether a crevasse can hydrofracture to the bed, not surface melt as previously thought by
278 Poinar and others (2017). Our observations of crevasse opening and the distribution of crevasse-nucleated
279 whaleback dunes indicate crevasses are forming over the firn aquifer, but their narrow surface widths sug-
280 gest they are not yet water-filled. While these crevasses are not presently draining the firn aquifer, future
281 changes in the magnitude of the local stress regime or in water table height could produce the conditions
282 required for crevasses forming in these higher-elevation areas to hydrofracture to the bed and drain the
283 firn aquifer. As a result, the downstream boundary of the firn aquifer could migrate to higher elevations,
284 allowing meltwater to access the bed in new, further inland regions. Given historical and ongoing climatic
285 warming, the inland migration of firn aquifer draining crevasses is likely a continuous process whereby
286 firn aquifer drainage crevasses have migrated to their present locations over the past 40+ years since their
287 formation in the 1980s (Miller and others, 2020).

288 **Requirements for firn aquifer drainage**

289 Our results demonstrate that the drainage of firn aquifers requires a balance between (1) dry crevasse depth
290 at the time of formation, (2) firn aquifer water table height, and (3) an influx of water to the crevasse
291 sufficient to drive the hydrofracturing process. Since Poinar and others (2017) studied point (3), we focus
292 on the first two requirements.

293 *Controls on dry crevasse depth*

294 The magnitude of applied stress exerts the strongest control on dry crevasse depth. We use primary
295 principal strain rates calculated from 1995–2010 multi-year ice velocities (Joughin and others, 2016) as
296 representative surface strain rates over our study area. The calculated values of surface stress are likely a
297 good approximation for the inland region of our profile where we expect the seasonal effects of subglacial
298 hydrology and stress perturbations from downstream fractures to be minimal. Calculated surface stress
299 values are likely too conservative in the three to eight kilometer region upstream of the main crevasse field,
300 where hydrologic connections can induce rapid or temporary changes to the stress field that are important
301 in creating new fractures (Gudmundsson, 2003). These transient stress perturbations are not resolved in
302 our derived stress field which is therefore likely too conservative because it does not capture transient

303 stress maxima. Induced stress perturbations would decay with distance from the hydrofractured crevasses
304 where they originate to produce the highest magnitude stresses in the region closest to the crevasse field.
305 Therefore, actual dry crevasse depths may be deeper than we predict, especially near known crevasse fields.

306 We find that the stress required to initiate fractures is 125-141 kPa, which is lower than observed
307 in some contexts (e.g., Ultee and others, 2020), but falls within the range of observations (Cuffey and
308 Paterson, 2010; Ultee, 2020; Vaughan, 1993). The values of surface stress presented here are calculated
309 with the creep parameter A for ice of -10°C (Cuffey and Paterson, 2010, p. 73). For a given strain rate,
310 the lower A values for colder, stiffer ice would produce a higher calculated stress, increasing our observed
311 yield strength of ice and producing deeper crevasses. Conversely, the higher A values for warmer, softer
312 ice would produce a lower calculated stress, decreasing our observed yield strength of ice and producing
313 shallower crevasses. We would expect a similar effect for using variable A for a vertical temperature profile
314 due to the warmer temperatures near the firn surface. For example, under an applied stress of 0.1 MPa our
315 base case model calculates a 17.4 m deep crevasse, changing A to $9.3 \times 10^{-25} \text{ Pa}^{-3} \text{ s}^{-1}$ for -5°C would lower
316 the applied stress by 0.028 MPa (28%) and reduce crevasse depth by 3.9 m (22%). We would therefore
317 expect dry crevasse depth to be shallower at the time of their formation if ice/firn temperatures were to
318 warm.

319 For the purposes of determining if a dry crevasse will reach the depth of a firn aquifer's water table, it
320 is important to consider the effect of low-density firn layer which can increase dry crevasse depth by up to
321 67%, however, the exact surface density value used is less important. Interspersing higher-density ice layers
322 within the firn pack increases ice density and produces a re-shallowing effect whereby dry crevasses are 4–
323 20% shallower. Our results agree with the work of Clayton and others (2024), who found the incorporation
324 of a low-density firn layer can increase crevasse depth by up to 20% for a thin glacier ($H \leq 250$ m). Even
325 though our work is applied to areas where the ice is thick ($H \geq 1,000$ m) and the effect of a surficial firn
326 layer will be minimized with depth, our focus on dry crevasse depth in the top 30–50 m reveals a similar
327 importance for incorporating the low density firn layer in LEFM modeling.

328 We account for the presence of multiple closely spaced crevasses by considering the shielding effect of
329 neighboring crevasses that dampens the far-field stress concentration at the crack tip (Sassolas and others,
330 1996). Without accounting for the effect of multiple crevasses, calculated dry crevasse depths would be 40–
331 90% too deep and would overpredict where crevasses should intersect the firn aquifer water table. Crevasse
332 fields with a greater spacing between neighboring crevasses would produce deeper crevasses which may

333 increase the likelihood of intersecting the aquifer water table. However, lower applied stresses would be
334 required for these crevasses to reach the same depth as another area with more closely spaced crevasses.
335 Crevasses located on the outer boundaries of a crevasse field can penetrate slightly deeper because they
336 are only shielded on one side (Clayton and others, 2022), potentially aiding the upglacier-most crevasses
337 in reaching the water table to initiate hydrofracture.

338 An increase in the fracture toughness of ice increases the applied stress required for the crevasse to
339 exist and reduces dry crevasse depth by 61–15% for applied stresses of 107–250 kPa. For $K_{IC} = 0.1$ MPa,
340 including a low-density firn layer reduces the applied stress required for a crevasse to exist by less than
341 27% (33–45 kPa) for a single crevasse, or 24% (35–46 kPa) for crevasses spaced 50 m apart. If the fracture
342 toughness of ice is increased to 0.4 MPa m^{-2} an applied stress 2.9 times larger, of 107 kPa, is required for
343 a crevasse to exist in the same conditions (Fig 4).

344 We find that our LEFM model produces deeper crevasses than the Nye depth (Fig. 10 in Appendix C.)
345 where crevasse depth is calculated as $T/\rho_i g$ where T is the traction stress acting to open the crevasse (Nye,
346 1954; Weertman, 1977). This result is expected and aligns with the analysis of Van Der Veen (1998) as the
347 Nye depth uses a constant ice density and is insensitive to crevasse spacing. For an applied stress less than
348 125 kPa the Nye criterion is similar to the model scenario with a constant ice density (Fig. 4a), for applied
349 stresses between 125 and 225 kPa the Nye criterion is similar to the model scenario where $K_{IC} = 0.4 \text{ MPa}$
350 $\text{m}^{1/2}$.

351 *Influence of firn aquifer hydrology on hydrofracture initiation*

352 For a crevasse to drain the firn aquifer it must penetrate deep enough to reach the water table which
353 supplies the water necessary to drive crevasse hydrofracture to the bed (Poinar and others, 2017). The
354 firn aquifer water table height responds to the magnitude of surface melt supplied as recharge and the
355 horizontal flux of water within the saturated zone as it is transported downslope following the hydraulic
356 gradient until draining into downstream crevasses. The firn aquifer water table varies over seasonal and
357 interannual timescales; thus, the critical dry fracture depth is also time-variable. The water table height is
358 closely tied to the slope of the snow surface, such that in steep areas the water table is deeper and in less
359 steeply sloping areas the water table is shallower (Miège and others, 2016). The depth to water table in
360 low-slope areas is consistently the shallowest along our profile and these areas experience more temporal
361 variability than steeper areas do (Fig. 3c–d).

362 On interannual timescales, aquifer water table height varies at a rate similar to that of surface mass
363 loss (Chu and others, 2018; Miège and others, 2016), whereby the water table height increases during high
364 melt intensity years and falls during subsequent years (Meyer and Hewitt, 2017; Miège and others, 2016;
365 Poinar and others, 2017). Notably, 2010–17 OIB detected water table locations demonstrate the aquifer's
366 water table can vary by over 10 m between years at a single location (Fig. 3). Crevasses formed during
367 years with high magnitude melting would be more likely to hydrofracture and drain the firn aquifer.

368 On seasonal timescales, meltwater recharge to the aquifer can raise the water table by up to four meters
369 (Miller and others, 2020), peaking in September after the end of the melt season. This lag between peak
370 melting and peak water table height likely reflects the lateral (downslope) flow of water within the aquifer
371 that continues after surface melting ceases for the year (Miège and others, 2016). A seasonal increase in
372 water table height of a few meters could determine whether a dry crevasse can hydrofracture to the bed,
373 particularly in the three regions identified as potential future aquifer drainage locations in Fig. 3. The
374 timing of dry crevasse formation may therefore play an important role in determining the inland migration
375 of aquifer drainage because dry crevasses are deepest immediately following their formation, before creep
376 closure causes the crevasse to shrink. The June 2023 crevasse opening event should have preceded the
377 period of rising water table which may have prevented this crevasse from intersecting the water table.
378 Crevasses that instead form during the fall may have an increased likelihood of reaching the water table and
379 hydrofracturing due to the higher water table from the full integrated melt accumulated over the summer
380 and the absence of snowfall. Although surficial meltwater discharge into crevasses has been suggested as
381 a requirement to begin aquifer drainage, we find that dry crevasses can penetrate the water table upon
382 formation to immediately initiate hydrofracture. Therefore, the timing of aquifer drainage would not be
383 constrained to the melt season but would still require the stress conditions conducive to fracturing.

384 **Inland migration of firn aquifer drainage**

385 The downstream boundary of the firn aquifer in our study area has been relatively steady (fluctuating
386 ± 2 km) since 2010 (Miège and others, 2016). Similarly, the locations of the widest crevasses, which are
387 hypothesized to drain firn aquifer water to the bed, have also been relatively steady (± 1 km) since 2010
388 (Fig. 1b; Poinar and others, 2017). Firn aquifer drainage has been thought to require surface generated
389 meltwater to begin the hydrofracturing process that then continues when crevasses penetrate deep enough
390 to access aquifer sourced discharge (McNerney, 2016). However, our modeling results indicate that surface

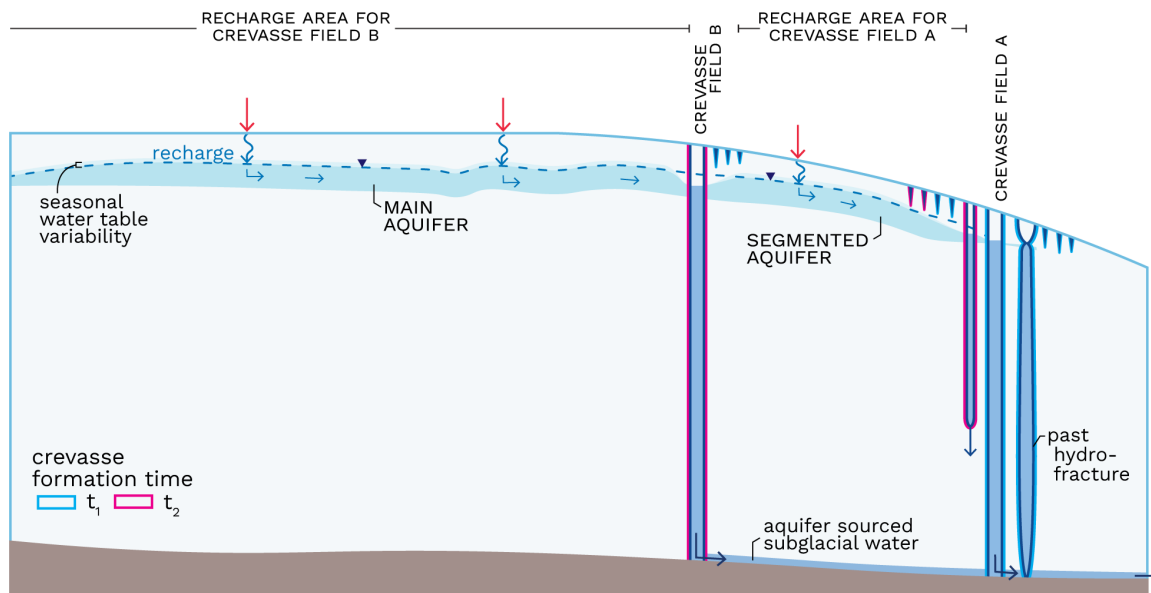


Fig. 8. Conceptual model of firn aquifer drainage inland migration (crevasse field B, time t_2) and segmented aquifer development (upstream of crevasse field A). Crevasses are outlined according to formation time with t_1 (cyan) and t_2 (magenta).

391 generated meltwater is not required to begin hydrofracturing, instead surface stresses can produce dry
 392 crevasses deep enough to intersect the firn aquifer water table. Crevasses that intersect the firn aquifer
 393 could immediately access the water required to initiate hydrofracture, regardless of the seasonal timing
 394 or availability of surface melt. Furthermore, our observations of crevasse-nucleated dunes and narrow
 395 crevasses at higher elevations than crevasses draining the firn aquifer indicate crevasses are forming in
 396 these further inland regions, but they are not propagating deep enough to intersect the water table. An
 397 increase in either the surface stresses or the aquifer water table height could enable firn aquifer drainage
 398 at higher elevations.

399 Along our transect on Helheim's southern branch, we identified three areas as potential future aquifer
 400 drainage locations where dry crevasses either reach or come within a meter of the OIB water table height
 401 (Fig. 3c–d). Crevasses formed in these areas could hydrofracture given a small (<1 m) increase in water
 402 table height, which is within the bounds of the expected seasonal and interannual variability of up to 4 m and
 403 10 m, respectively (Miège and others, 2016; Miller and others, 2020). In response to the inland migration
 404 of firn aquifer draining crevasses, the firn aquifer could either recede inland and abandon downstream
 405 crevasses or the aquifer could become segmented such that smaller aquifers occupy compressional areas
 406 and drain into downstream crevasses (Fig. 8). We would expect the latter scenario as long as the region

407 between full-thickness crevasses is sufficiently large and maintains a thick firn layer, so that sustained
408 aquifer recharge between crevasse fields can keep the smaller aquifers intact. This concept of a segmented
409 firn aquifer would explain observations of small, isolated firn aquifers located between crevasse fields at
410 lower elevations (Miège and others, 2016).

411 The inland migration of firn aquifer drainage would allow aquifer-sourced water to reach new areas of the
412 bed to affect the structure of, and pressures within, the subglacial drainage system that controls sliding. In a
413 scenario where full-thickness crevasses form in region 1 (Fig. 3), water would enter the subglacial drainage
414 system 7.8–11.6 km further inland than it currently does. The movement of the injection point would
415 increase subglacial water pressure at the inland location while potentially decreasing pressures downstream
416 according to idealized simulations by Poinar and others (2019), which suggested that this change in water
417 pressure is long-lasting (>4 years). However, how the downstream subglacial drainage system will respond
418 to the inland migration of firn aquifer drainage is unresolved. We would expect subglacial pressurization,
419 and therefore elevated ice velocities, to expand inland resulting in a larger area exposed to higher subglacial
420 water pressures than at present. The increased basal lubrication and higher sliding speeds would likely raise
421 wintertime or “background” sliding speeds that are used as a baseline to measure seasonal, melt-induced
422 velocity changes against (Sommers and others, 2023). Consequences of higher winter sliding speeds, in
423 terms of ice sheet mass loss, could be magnified as firn aquifer drainage migrates further inland and as
424 higher wintertime velocities persist if they are not compensated for by summertime slowdowns at lower
425 elevations.

426 These surface-to-bed connections are particularly important because firn aquifers have expanded and
427 can continue to expand inland under enhanced melting (Horlings and others, 2022; Miège and others, 2016;
428 Steger and others, 2017a). By constraining the conditions required for crevasses to drain firn aquifers, dry
429 crevasse depth and aquifer water table height, we find that the location of aquifer-draining crevasses can,
430 and as evidenced by the detection of crevasse formation over the firn aquifer, may already be in the process
431 of migrating inland. For these reasons, future work should assess the impact of firn aquifer drainage at
432 higher elevations on subglacial hydrology and ice dynamics.

433 CONCLUSIONS

434 Our findings suggest that crevasses formed over a firn aquifer on Helheim Glacier can reach the water
435 table depth to initiate hydrofracture without surface meltwater inputs. We identify inland areas that are

436 the most vulnerable to full thickness hydrofracture given rises in the firn aquifer water table, increases in
437 surface stresses, or both. These full-thickness crevasses would drain aquifer water to the bed at new inland
438 locations, moving the downstream boundary of the aquifer inland. This inland expansion may be underway
439 as evidenced by our in situ observations of a crevasse opening event 4 km from the main crevasse field and
440 of crevasse-nucleated whaleback dunes expanding 14 km inland from the main crevasse field in 2023. New
441 surface-to-bed connections at even higher elevations than those observed presently would allow meltwater
442 to access new regions of the bed with potentially significant impacts on downstream subglacial hydrology
443 and ice sliding velocity.

444 ACKNOWLEDGEMENTS

445 This project was supported by the Heising-Simons Foundation grant numbers 2020-1909, 2020-1910 and
446 2020-1911 as well as by the Army Research Office #78811EG (crm). We thank M. Coyle, R. Mansfield,
447 I. McDowell, C. Shafer, A. Tarzona, T. J. Young, R. Clavette, and B. Horlings for their contributions
448 to fieldwork. We also thank L. Stearns for their support during field endeavors. Geospatial support
449 for this work provided by the Polar Geospatial Center under NSF-OPP awards 1043681, 1559691, and
450 2129685. ArcticDEM v4.1 provided by the Polar Geospatial Center under NSF-OPP awards 1043681,
451 1559691, 1542736, 1810976, and 2129685. Data from the Programme for Monitoring of the Greenland
452 Ice Sheet (PROMICE) are provided by the Geological Survey of Denmark and Greenland (GEUS) at
453 <http://www.promice.dk>.

454 REFERENCES

- 455 Bartholomew ID, Nienow PW, Sole AJ, Mair DW, Cowton T, King MA and Palmer S (2011) Seasonal variations
456 in Greenland Ice Sheet motion: Inland extent and behaviour at higher elevations. *Earth and Planetary Science*
457 *Letters*, **307**(3-4), 271–278, ISSN 0012821X (doi: 10.1016/j.epsl.2011.04.014)
- 458 Chu W, Schroeder DM and Siegfried MR (2018) Retrieval of Englacial Firn Aquifer Thickness From Ice-Penetrating
459 Radar Sounding in Southeastern Greenland. *Geophysical Research Letters*, **45**(21), 11,770–11,778, ISSN 19448007
460 (doi: 10.1029/2018GL079751)
- 461 Cicero E, Poinar K, Jones-Ivey R, Petty AA, Sperhac JM, Patra A and Briner JP (2023) Firn aquifer water
462 discharges into crevasses across Southeast Greenland. *Journal of Glaciology*, **40**(1), 1–14, ISSN 00221430 (doi:
463 10.1017/jog.2023.25)

- 464 Clayton T, Duddu R, Siegert M and Martínez-Pañeda E (2022) A stress-based poro-damage phase field model for
465 hydrofracturing of creeping glaciers and ice shelves. *Engineering Fracture Mechanics*, **272**(July), 108693, ISSN
466 00137944 (doi: 10.1016/j.engfracmech.2022.108693)
- 467 Clayton T, Duddu R, Hageman T and Martinez-Paneda E (2024) The influence of firn-layer material properties on
468 surface crevasse propagation in glaciers and ice shelves. *EGUsphere*, **2024**, 1–28
- 469 Cuffey KM and Paterson WSB (2010) *The physics of glaciers*, 19,73. Academic Press, 4th ed. edition
- 470 Doyle SH, Hubbard A, Fitzpatrick AAW, As DV, Mikkelsen APB, Pettersson R and Hubbard B (2014) Persistent
471 flow acceleration within the interior of the Greenland ice sheet. *Geophysical Research Letters*, **41**(April), 899–905,
472 ISSN 19448007 (doi: 10.1002/2014GL061184)
- 473 Fausto RS, van As D, Mankoff KD, Vandecrux B, Citterio M, Ahlstrøm AP, Andersen SB, Colgan W, Karlsson NB,
474 Kjeldsen KK and others (2021) Programme for Monitoring of the Greenland Ice Sheet (PROMICE) automatic
475 weather station data. *Earth System Science Data*, **13**(8), 3819–3845
- 476 Filhol S and Sturm M (2015) Snow bedforms: A review, new data, and a formation model. *Journal of Geophysical*
477 *Research: Earth Surface*, **120**, 1645–1669 (doi: doi:10.1002/ 2015JF003529)
- 478 Forster RR, Box JE, van den Broeke MR, Miège C, Burgess EW, van Angelen JH, Lenaerts JTM, Koenig LS, Paden
479 JD, Lewis C, Gogineni SP, Leuschen C and McConnell JR (2014) Extensive liquid meltwater storage in firn within
480 the Greenland ice sheet. *Nature Geoscience*, **7**(2), 1–4, ISSN 1752-0894 (doi: 10.1038/ngeo2043)
- 481 Global Modeling and Assimilation Office (2015) Merra-2 `statd_2d_slv_nx`: 2d, daily, aggregated statistics, single-
482 level, assimilation, single-level diagnostics. *Goddard Earth Sciences Data and Information Services Center (GES*
483 *DISC)* (doi: 10.5067/9SC1VNTWGWW3)
- 484 Gudmundsson GH (2003) Transmission of basal variability to a glacier surface. *Journal of Geophysical Research:*
485 *Solid Earth*, **108**(B5), 1–19 (doi: 10.1029/2002jb002107)
- 486 Gulley JD, Grabiec M, Martin JB, Jania J, Catania GA and Glowacki PS (2012) The effect of discrete recharge by
487 moulins and heterogeneity in flow-path efficiency at glacier beds on subglacial hydrology. *Journal of Glaciology*,
488 **58**(211), 926–940, ISSN 00221430 (doi: 10.3189/2012JoG11J189)
- 489 Herring T, King RW and McClusky SC (2010) Introduction to GAMIT/GLOBK. *Mass. Inst. of Technol., Cambridge,*
490 *Mass*
- 491 Horlings AN, Christianson K and Miège C (2022) Expansion of firn aquifers in southeast greenland. *Journal of*
492 *Geophysical Research: Earth Surface*, **127**(10), e2022JF006753

- 493 How P, Abermann J, Ahlstrøm A, Andersen S, Box JE, Citterio M, Colgan W, RS F, Karlsson N, Jakobsen J,
494 Langley K, Larsen S, Lund M, Mankoff K, Pedersen A, Rutishauser A, Shield C, Solgaard A, van As D, Vandecrux
495 B and Wright P (2022) PROMICE and GC-Net automated weather station data in Greenland. *GEUS Dataverse*
496 (doi: 10.22008/FK2/IW73UU)
- 497 Howat IM, Negrete A and Smith BE (2014) The Greenland Ice Mapping Project (GIMP) land classification and
498 surface elevation data sets. *The Cryosphere*, **8**(4), 1509–1518 (doi: 10.5194/tc-8-1509-2014)
- 499 Joughin I, Smith B, Howat I and Scambos T (2016) Measures multi-year greenland ice sheet velocity mosaic, version
500 1. Boulder, Colorado USA. NASA National Snow and Ice Data Center Distributed Active Archive Center. (doi:
501 <https://doi.org/10.5067/QUA5Q9SVMSJG>)
- 502 Kobayashi S (1980) Studies on interaction between wind and dry snow surface. *Contributions from the Institute of*
503 *Low Temperature Science*, **29**, 1–64
- 504 Li S and Sturm M (2002) Patterns of wind-drifted snow on the Alaskan arctic slope, detected with ERS-1 interfero-
505 metric SAR. *Journal of Glaciology*, **48**(163), 495–504, ISSN 00221430 (doi: 10.3189/172756502781831151)
- 506 Maxar (2021) Accuracy of worldview products. Last accessed 24 March 2024
- 507 McNerney L (2016) *Constraining the Greenland Firn Aquifer's Ability to Hydrofracture a Crevasse to the Bed of the*
508 *Ice Sheet*. Masters thesis, University of Utah
- 509 Mejia JZ, Gulley J, Trunz C, Covington MD, Bartholomaeus TC, Breithaupt CI, Xie S and Dixon TH (2022) Moulin
510 density controls the timing of peak pressurization within the Greenland Ice Sheet's subglacial drainage system.
511 *Geophysical Research Letters*, **49**, 1–13 (doi: <https://doi.org/10.1002/essoar.10511864.1>)
- 512 Meyer CR and Hewitt IJ (2017) A continuum model for meltwater flow through compacting snow. *Cryosphere*, **11**(6),
513 2799–2813, ISSN 19940424 (doi: 10.5194/tc-11-2799-2017)
- 514 Meyer CR and Minchew BM (2018) Temperate ice in the shear margins of the antarctic ice sheet: Controlling
515 processes and preliminary locations. *Earth and Planetary Science Letters*, **498**, 17–26
- 516 Miège C, Forster RR, Brucker L, Koenig LS, Solomon DK, Paden JD, Box JE, Burgess EW, Miller JZ, McNerney L,
517 Brautigam N, Fausto RS and Gogineni S (2016) Spatial extent and temporal variability of Greenland firn aquifers
518 detected by ground and airborne radars. *Journal of Geophysical Research: Earth Surface*, **121**(12), 2381–2398,
519 ISSN 21699011 (doi: 10.1002/2016JF003869)
- 520 Miller O, Solomon DK, Miège C, Koenig L, Forster R, Schmerr N, Ligtenberg SR and Montgomery L (2018) Direct
521 Evidence of Meltwater Flow Within a Firn Aquifer in Southeast Greenland. *Geophysical Research Letters*, **45**(1),
522 207–215, ISSN 19448007 (doi: 10.1002/2017GL075707)

- 523 Miller O, Solomon DK, Miège C, Koenig L, Forster R, Schmerr N, Ligtenberg SR, Legchenko A, Voss CI, Montgomery
524 L and McConnell JR (2020) Hydrology of a Perennial Firn Aquifer in Southeast Greenland: An Overview Driven
525 by Field Data. *Water Resources Research*, **56**(8), ISSN 19447973 (doi: 10.1029/2019WR026348)
- 526 Miller OL, Solomon DK, Miège C, Koenig LS, Forster RR, Montgomery LN, Schmerr N, Ligtenberg SR, Legchenko A
527 and Brucker L (2017) Hydraulic conductivity of a Firn aquifer in southeast Greenland. *Frontiers in Earth Science*,
528 **5**(May), 1–13, ISSN 22966463 (doi: 10.3389/feart.2017.00038)
- 529 Minchew BM, Meyer CR, Robel AA, Gudmundsson GH and Simons M (2018) Processes controlling the downstream
530 evolution of ice rheology in glacier shear margins: case study on rutford ice stream, west antarctica. *Journal of*
531 *Glaciology*, **64**(246), 583–594
- 532 Miège C (2018) Spatial extent of greenland firn aquifer detected by airborne radars, 2010-2017. *Arctic Data Center*
533 (doi: 10.18739/A2TM72225)
- 534 Montgomery LN, Schmerr N, Burdick S, Forster RR, Koenig L, Legchenko A, Ligtenberg S, Miège C, Miller OL
535 and Solomon DK (2017) Investigation of firn aquifer structure in southeastern Greenland using active source
536 seismology. *Frontiers in Earth Science*, **5**(February), 1–12, ISSN 22966463 (doi: 10.3389/feart.2017.00010)
- 537 Morlighem M, Williams CN, Rignot E, An L, Arndt JE, Bamber JL, Catania G, Chauché N, Dowdeswell JA, Dorschel
538 B and others (2017) Bedmachine v3: Complete bed topography and ocean bathymetry mapping of greenland from
539 multibeam echo sounding combined with mass conservation. *Geophysical Research Letters*, **44**(21), 11–051
- 540 Nye JF (1954) Comments on Dr. Loewe's Letter and Notes on Crevasses. *Journal of Glaciology*, **1**(5), 625–628
- 541 Phillips T, Leyk S, Rajaram H, Colgan W, Abdalati W, McGrath D and Steffen K (2011) Modeling moulin distribution
542 on Sermeq Avannarleq glacier using ASTER and WorldView imagery and fuzzy set theory. *Remote Sensing of*
543 *Environment*, **115**(9), 2292–2301, ISSN 00344257 (doi: 10.1016/j.rse.2011.04.029)
- 544 Poinar K and Andrews L (2021) Challenges in predicting Greenland supraglacial lake drainages at the regional scale.
545 *Cryosphere*, **15**(3), 1455–1483, ISSN 19940424 (doi: 10.5194/tc-15-1455-2021)
- 546 Poinar K, Joughin I, Das SB, Behn MD, Lenaerts JTM and van den Broeke MR (2015) Limits to future expansion
547 of surface-melt-enhanced ice flow into the interior of western Greenland. *Geophysical Research Letters*, **42**(6),
548 1800–1807, ISSN 19448007 (doi: 10.1002/2015GL063192)
- 549 Poinar K, Joughin I, Lilien D, Brucker L, Kehrl L and Nowicki S (2017) Drainage of southeast Greenland firn aquifer
550 water through crevasses to the bed. *Frontiers in Earth Science*, **5**, ISSN 22966463 (doi: 10.3389/feart.2017.00005)

- 551 Poinar K, Dow CF and Andrews LC (2019) Long-Term Support of an Active Subglacial Hydrologic System in
552 Southeast Greenland by Firn Aquifers. *Geophysical Research Letters*, **46**(9), 4772–4781, ISSN 0094-8276 (doi:
553 10.1029/2019gl082786)
- 554 Porter C, Howat I, Noh M, Husby E, Khuvis S, Danish E, Tomko K, Gardiner J, Negrete A, Yadav B, Klassen J,
555 Kelleher C, Cloutier M, Bakker J, Enos J, Arnold G, Bauer G and Morin P (2023) ArcticDEM. *Harvard Dataverse*,
556 **V1, Version 4.1**
- 557 Rienecker MM, Suarez MJ, Gelaro R, Todling R, Bacmeister J, Liu E, Bosilovich MG, Schubert SD, Takacs L, Kim
558 GK and others (2011) Merra: Nasa’s modern-era retrospective analysis for research and applications. *Journal of*
559 *Climate*, **24**(14), 3624–3648
- 560 Sassolas C, Pfeffer T and Amadei B (1996) Stress interaction between multiple crevasses in glacier ice. *Cold Regions*
561 *Science and Technology*, **24**(2), 107–116, ISSN 0165232X (doi: 10.1016/0165-232X(96)00002-X)
- 562 Sommers A, Meyer CR, Morlighem M, Rajaram H, Poinar K, Chu W and Mejia JZ (2023) Subglacial hydrology
563 modeling predicts high winter water pressure and spatially variable transmissivity at Helheim Glacier, Greenland.
564 *Journal of Glaciology*, 1–13 (doi: <https://doi.org/10.31223/X5RD24>)
- 565 Sommers AN, Meyer CR, Poinar K, Mejia J, Morlighem M, Rajaram H, Warburton K and Chu W (2024) Helheim
566 velocity controlled both by terminus effects and subglacial hydrology with distinct realms of influence. *Authorea*
567 *Preprints*
- 568 Steger CR, Reijmer CH and Van Den Broeke MR (2017a) The modelled liquid water balance of the Greenland Ice
569 Sheet. *Cryosphere*, **11**(6), 2507–2526, ISSN 19940424 (doi: 10.5194/tc-11-2507-2017)
- 570 Steger CR, Reijmer CH, Van Den Broeke MR, Wever N, Forster RR, Koenig LS, Kuipers Munneke P, Lehning M,
571 Lhermitte S, Ligtenberg SR and others (2017b) Firn meltwater retention on the greenland ice sheet: A model
572 comparison. *Frontiers in Earth Science*, **5**, 3
- 573 Ultee L (2020) SERMeQ Model Produces a Realistic Upper Bound on Calving Retreat for 155 Greenland Outlet
574 Glaciers. *Geophysical Research Letters*, **47**, 1–10 (doi: 10.1029/2020GL090213)
- 575 Ultee L, Meyer C and Minchew B (2020) Tensile strength of glacial ice deduced from observations of the 2015 eastern
576 Skaftá cauldron collapse, Vatnajökull ice cap, Iceland. *Journal of Glaciology*, **66**(260), 1024–1033, ISSN 00221430
577 (doi: 10.1017/jog.2020.65)
- 578 van den Broeke MR, Kuipers Munneke P, Noël B, Reijmer C, Smeets P, van de Berg WJ and van Wessem JM (2023)
579 Contrasting current and future surface melt rates on the ice sheets of Greenland and Antarctica: Lessons from in
580 situ observations and climate models. *PLOS Climate*, **2**(5), 1–17 (doi: 10.1371/journal.pclm.0000203)

- 581 Van Der Veen CJ (1998) Fracture mechanics approach to penetration of bottom crevasses on glaciers. *Cold Regions*
 582 *Science and Technology*, **27**(3), 213–223, ISSN 0165232X (doi: 10.1016/S0165-232X(98)00006-8)
- 583 van der Veen CJ (2007) Fracture propagation as means of rapidly transferring surface meltwater to the base of
 584 glaciers. *Geophysical Research Letters*, **34**(1), 1–5, ISSN 00948276 (doi: 10.1029/2006GL028385)
- 585 Vaughan DG (1993) Relating the occurrence of crevasses to surface strain rates. *Journal of Glaciology*, **39**(132),
 586 255–266, ISSN 00221430 (doi: 10.1017/S0022143000015926)
- 587 Weertman J (1977) Penetration Depth of Closely Spaced Water-free Crevasses. *Journal of Glaciology*, **18**(78), 37–46
- 588 Yang K and Smith LC (2016) Internally drained catchments dominate supraglacial hydrology of the southwest Green-
 589 land Ice Sheet. *Journal of Geophysical Research : Earth Surface*, **121**, 1891–1910 (doi: doi:10.1002/ 2016JF003927)

590 APPENDIX A – EXTENDED METHODOLOGY

591 On-ice GNSS station pairs

592 In 2023 we installed eight GNSS stations in a strain diamond configuration extending 4 km along flow
 593 from our field camp to the crevasse field draining the firn aquifer, and 1 km in the across-flow direction
 594 (Fig. 1). Each station was equipped with a Trimble NetR9 receiver, recording at 15 second intervals,
 595 and a Zephyr Geodetic Antenna mounted to aluminum conduit installed within the snow and stabilized
 596 with snow anchors and guy lines. We process positions using the GNSS base station HEL2 (66.40116°N,
 597 -38.21570°E) mounted on bedrock near the terminus of Helheim Glacier, with a baseline length of 41 km.
 598 We determine kinematic site positions for on-site stations using carrier-phase differential processing relative
 599 to HEL2, implemented with TRACK software (Herring and others, 2010). Kinematic positions for each
 600 station were resolved at 30 second intervals to match the sampling rate of our base station HEL2. Station
 601 position timeseries has a formal error of ~2 cm in the horizontal direction.

We calculate shear stress (σ) from the GNSS-station derived strain rate ($\dot{\epsilon}$) following Glen's Law,

$$\sigma = \sqrt[n]{\frac{\dot{\epsilon}}{A}} = \sqrt[3]{\frac{\dot{\epsilon}}{A}} \quad (\text{A1})$$

602 where n is the flow law exponent taken to be $n = 3$, and A is the creep parameter. We use A for ice
 603 temperature $T = -10^\circ\text{C}$ where $A = 3.5 \times 10^{-25} \text{ Pa}^{-3}\text{s}^{-1}$.

604 *Principal strain rates and surface stresses*

605 We calculate primary principal strain rates using NASA MEaSUREs program Multi-year Greenland Ice
 606 Sheet Velocity Mosaic (Joughin and others, 2016) velocities. This velocity product comprises a year-round
 607 velocity average that is selected to be representative of the 1995–2015 period and has a pixel size of 250
 608 m by 250 m. We smooth the velocities with a 1 km² Savitzky-Golay filter to derive two-dimensional
 609 principal strain rates over Helheim Glacier (cf. Meyer and Minchew, 2018; Minchew and others, 2018;
 610 Poinar and Andrews, 2021). Here we use the more extensional principal strain rate ($\dot{\epsilon}_3$) alongside the more
 611 compressional principal strain rate ($\dot{\epsilon}_1$) and the shear strain rate ($\dot{\epsilon}_{xy}$). Shear stress along the OIB firn
 612 aquifer profile is calculated as:

$$\sigma_3 = \frac{1}{A^{\frac{1}{n}}} \dot{\epsilon}_{eff}^{\frac{1-n}{n}} \dot{\epsilon}_3 \quad (\text{A2})$$

where the creep exponent is $n=3$, the creep parameter is $A=3.5 \times 10^{-25} \text{ Pa}^{-3} \text{ s}^{-1}$ for ice temperature of -10°C , for effective strain rate

$$\dot{\epsilon}_{eff} = \sqrt{\frac{1}{2}(\dot{\epsilon}_1^2 + \dot{\epsilon}_3^2) + \dot{\epsilon}_{xy}^2} \quad (\text{A3})$$

613 **Air temperatures**

614 To approximate when the snow surface in our study area first reached the melting point in 2023, we
 615 use MERRA-2 climate reanalysis data (Rienecker and others, 2011). We start with the MERRA-2 daily
 616 aggregated statistics single-level diagnostics data (M2SDNXSLV; Global Modeling and Assimilation Office,
 617 2015) for 2-meter air temperature on the MERRA-2 grid. These data are spaced by 0.5° latitude and
 618 0.625° longitude, or ~ 55 km by ~ 42 km at our study area. To calculate air temperature at our field camp
 619 (surface elevation $s=1,536$ m), we regress MERRA-2 daily minimum, mean, and maximum temperatures
 620 against surface elevation at the five closest grid points to camp (Fig. 5). The centers of these grid boxes
 621 span surface elevations from 1,270 m to 2,015 m and are located 19 km ($s=1,770$ m) to 44 km ($s=1,480$
 622 m) from our field camp.

623 **Wind direction at weather station NSE**

624 We compare dune orientation to wind direction data at the closest PROMICE weather station, NSE, located
 625 at 2,375 m a.s.l, 150 km west of our study area (Fausto and others, 2021; How and others, 2022). We use

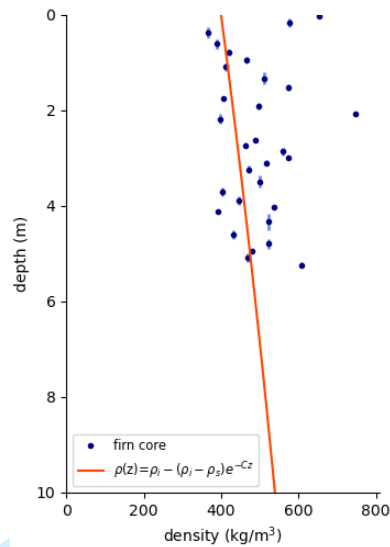


Fig. 9. Firn core measurements and depth-density relation fit (red) for $\rho_s = 400 \text{ kg m}^{-3}$ and $C = 0.0314 \text{ m}^{-1}$. Navy dots mark the mid-point of the depth range for that given density and light blue lines mark the full depth range for a density measurement.

626 daily averaged weather station observations collected between 19 June 2021 through 8 February 2024. We
 627 resolve the wind direction during dune formation events by filtering the dataset to observations ($n = 357$)
 628 with wind speeds greater than 15 m s^{-1} as required for whaleback dune formation (Filhol and Sturm,
 629 2015). Wind directions were within 129° – 138° representing 21% of all high-wind observations (Fig. 6c).

630 **Firn Density**

To constrain the empirical snow density-depth formulation, $\rho(z)$, used to calculate the overburden pressure acting on the walls of crevasses in our LEFM model in Appendix B, we measured snow density in June 2023 from a 6-m firn core collected at our field site over the firn aquifer (Figs. 1b, 9). Snow density as a function of depth is calculated following (Cuffey and Paterson, 2010, p. 19):

$$\rho(z) = \rho_i - (\rho_i - \rho_s)e^{-Cz} \quad (\text{A4})$$

631 where z is depth below the surface in meters, ρ_i is ice density taken to be 917 kg m^{-3} , ρ_s is surface snow
 632 density, usually within the range of 300 to 400 kg m^{-3} . C is a site-specific empirical constant that ranges
 633 from 0.0165 to 0.0314 m^{-1} . The snowpack exhibited high variability with depth; conditions ranged from
 634 sugar snow to ice and melt layers. We obtained values for ρ_s and C by least-squares fitting the data. We

635 find a best fit of the snow density-depth formulation to our data occurs with a surface density $\rho_s=400$ kg
 636 m^{-3} and $C=0.0314 \text{ m}^{-1}$, and use these values in Eq. B4 in Appendix B.

637 APPENDIX B – MODEL FORMULATION

638 Here we follow van der Veen (2007) for the penetration depth of a water-free crevasse, solving for the net
 639 stress intensity factor (K_I^{NET}) by setting it equal to the fracture toughness of ice K_{IC} taken here as 0.1
 640 MPa $\text{m}^{1/2}$.

$$K_I^{NET} = K_I^{(1)} + K_I^{(2)} = K_{IC} \quad (\text{B1})$$

K_I^{NET} is the sum of the tensile $K_I^{(1)}$ and lithostatic $K_I^{(2)}$ stress components. For closely spaced crevasses
 we calculate the the stress intensity factor for crevasse opening due to a constant tensile stress following
 (Van Der Veen, 1998):

$$K_I^{(1)} = D(S)R_{xx}\sqrt{\pi dS} \quad (\text{B2})$$

$$D(S) = \frac{1}{\sqrt{\pi}} \left[1 + \frac{1}{2}S + \frac{3}{8}S^2 + \frac{6}{16}S^3 + \frac{35}{128}S^4 + \frac{63}{256}S^5 + \frac{231}{1024}S^6 \right] + 22.5S^7 - 63.5S^8 + 58.05S^9 - 17.58S^{10} \quad (\text{B3})$$

641 where R_{xx} is the far-field resistive stress, d is crevasse depth, $S = \frac{W}{W+d}$ where the spacing between neigh-
 642 boring crevasses is $2W$. We use $2W = 50$ m which is derived from the mean crevasse spacing in the main
 643 crevasse field along in our study area (Fig. 1c). $D(S)$ describes the effect of shielding when more than one
 644 crevasse is present as in the case of the closely spaced crevasses characteristic of Helheim Glacier.

645 Crevasse closure due to ice overburden pressure is accounted for by calculating $K_I^{(2)}$ which yields the
 646 stress intensity factor for the weight of the overlying ice as:

$$K_I^{(2)} = \frac{2\rho_i g}{\sqrt{\pi d}} \int_0^d \left[-z + \frac{\rho_i - \rho_s}{\rho_i C} (1 - e^{-Cz}) \right] G(\gamma, \lambda) dz \quad (\text{B4})$$

$$G(\gamma, \lambda) = \frac{3.52(1 - \gamma)}{(1 - \lambda)^{3/2}} - \frac{4.35 - 5.28\gamma}{(1 - \lambda)^{1/2}} + \left[\frac{1.3 - 0.3\gamma^{3/2}}{(1 - \gamma)^{1/2}} + 0.83 - 1.76\gamma \right] \times [1 - (1 - \gamma)\lambda] \quad (\text{B5})$$

647 where H is ice thickness, $\gamma = z/d$, $\lambda = d/H$. We account for the presence of a low-density firn layer at the
 648 surface using the relationship in (A4), where $\rho_s = 400 \text{ kg m}^{-3}$ and $C = 0.0314 \text{ m}^{-1}$ whose determination
 649 is discussed in Appendix A.

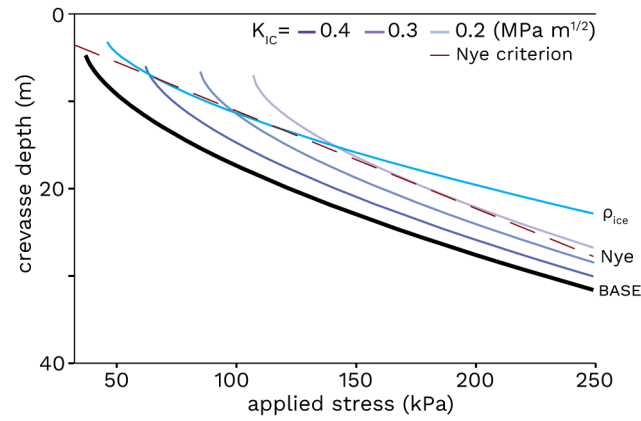


Fig. 10. Nye criterion crevasse depth comparison. Same as in Fig. 4a but with the Nye criterion in a red dashed line. Our base case is shown in bold ($\rho_s=400 \text{ kg m}^{-3}$, $K_{IC}=0.1 \text{ MPa}$, $2W=50 \text{ m}$). Purple lines show model runs with variable K_{IC} and the cyan line shows a constant density solution where $\rho_s = \rho_i$.

650 APPENDIX C – NYE CRITERION

651 We compare our model results to the Nye criterion for crevasse depth (Nye, 1954; Weertman, 1977) which
652 is shown in Figure 10. For closely-spaced, water-free crevasses the Nye criterion states that crevasse depth

653 L is

$$L = \frac{T}{\rho_i g} \quad (\text{C1})$$

654 where T is the tensile stress within the ice, ρ_i is the density of ice taken to be 917 kg m^{-3} , and g is
655 acceleration due to gravity of 9.81 m s^{-2} .